Research Article Vol. 3, No. 3 / 25 June 2025 / Optica Quantum 295

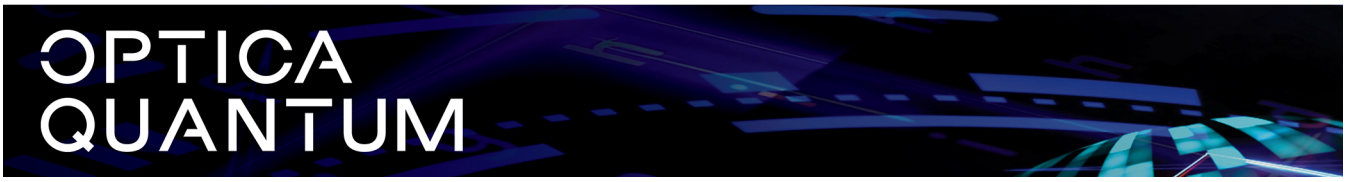

Efficient storage of multidimensional telecom photons in a solid-state quantum memory

Zongfeng Li,[1] Yisheng Lei,[1] Trevor Kling,[1] and Mahdi Hosseini[1,2,*]

[1]Department of Electrical and Computer Engineering and Applied Physics Program, Northwestern University, Evanston, Illinois 60208, USA
[2]Elmore Family School of Electrical and Computer Engineering, Purdue University, West Lafayette, Indiana 47907, USA
*mh@northwestern.edu

Received 7 April 2025; revised 27 May 2025; accepted 28 May 2025; published 24 June 2025

Efficient storage of telecom-band quantum optical information represents a crucial milestone for establishing distributed quantum optical networks. Erbium ions in crystalline hosts provide a promising platform for telecom quantum memories; however, their practical applications have been hindered by demanding operational conditions, such as ultra-high magnetic fields and ultra-low temperatures. In this work, we demonstrate the storage of telecom photonic qubits encoded in polarization, frequency, and time-bin bases. Using the atomic frequency comb protocol in an Er^{3+}-doped crystal, we developed a memory initialization scheme that improves storage efficiency by over an order of magnitude. The observed results were made possible by the deliberate selection of the pumping sequence and the minimization of lattice interactions, to the extent possible without the use of dilution refrigerators or superconducting magnets.

https://doi.org/10.1364/OPTICAQ.564321

1. INTRODUCTION

Optical quantum networks have numerous proposed applications such as distributed quantum computing, blind quantum computing, secure communications, and distributed quantum sensing [1,2]. Due to the exponential optical loss in optical fibers and the fundamental inability of quantum information amplification, quantum memory devices are sought to relay and synchronize quantum information distributed over long distances [3–5]. To enable long-range networking, various quantum repeater schemes have been proposed [4,6–8]. Quantum repeaters based on absorptive quantum memories have the potential advantages of long-life storage [9], multiplexed operations [10–13], photonic integration [14], and interfacing with ubiquitous entanglement sources [15–17]. In addition, quantum memories have other applications including, but not limited to, single-photon generation [18], multi-photon synchronization [19,20], linear optical quantum computing [21], quantum sensing [22,23], and fundamental science in space [24].

Quantum memories with rare-earth ions in solids are under active development [5,14,25]. Elementary quantum networks have been demonstrated with rare-earth-ion ensembles in crystals interfaced with entangling photon sources and wavelength conversion to accommodate memory wavelength, which is mostly outside the telecom band [15,16]. Typically, the atomic frequency comb (AFC) protocol [26] is employed for storage. Erbium ions, Er^{3+}, in solids have optical transitions in the telecom C-band, an unparalleled property that is suitable for integration with existing optical fiber networks. Over 1 s coherence time of nuclear spin in a high magnetic field and milliseconds in zero field has been reported with an Er^{3+}:YSO crystal [27,28], and memory-source integration has been demonstrated as well [29]. Using Er^{3+}:$CaWO_4$ crystals, an electronic spin coherence time of 23 ms has been observed [30], and single spin-photon entanglement has been demonstrated [31]. The practical deployment of Er-doped solids as quantum memories enables advancements beyond passive memory elements [32], significantly extending communication distances, while offering a platform for deterministic entanglement and coherent control of information.

The recent development in Er crystals has relied on dilution refrigeration or high magnetic fields (approximately 7 Tesla) to achieve certain memory milestones. The presence of a half-integer spin in Er^{3+} ions demands both low temperatures and a high magnetic field to freeze the coherence-degrading spin-flip transitions [27]. Additionally, the low branching ratio, that is, the electrons in the excited state tend to return to their original ground state rather than other spin ground states, and the presence of a large number of hyperfine states complicate the spectral tailoring features in erbium [33] compared with other ion candidates. For these reasons, the initialization and operation of Er-based quantum memories has proved difficult posing limitations on its practical deployment when it comes to multiplexed processing.

A storage efficiency of up to 22% has been observed in an ^{167}Er:YSO crystal with a 7-T field at 1.5 K [34]. Other approaches have used a moderate magnetic field in a dilution refrigerator to achieve the same spin-freezing, but with a much lower storage efficiency of 0.2% [35]. Multimode quantum storage with erbium-doped fibers at 10 mK (dilution refrigerator) have been demonstrated [36]; however, it suffers from

low storage efficiency and short storage time. Despite significant advancements in telecom quantum memory development, achieving a scalable solution for practical quantum optical networks requires overcoming the reliance on ultra-high magnetic fields and dilution refrigerators.

In this article, we report the development of an efficient and multidimensional quantum storage in an AFC quantum memory based on an Er^{3+}:YSO crystal, without using superconducting magnets or a dilution refrigerator. We develop a simple but efficient spectral hole pumping method to perform the spectral tailing required for the AFC storage in the telecom band. We demonstrate the storage and retrieval of single photons in polarization, frequency, and time-bin basis. Memory fidelity was evaluated using quantum process tomography for polarization qubits and intensity noise estimation for frequency and time-bin qubits.

2. EXPERIMENT

The 0.005% ^{167}Er:YSO crystal dimensions are 2 mm × 3 mm × 4 mm, with the b-axis aligned with the 4 mm edge. Both the D_1 and D_2 axes are in the 2 mm × 3 mm plane, at a 45° angle to the crystal edges. The magnetic field is orientated along the 3 mm edge, which gives a nearly maximum electron Zeeman splitting [37]. Additionally, defects in the host YSO materials produce fluctuations in the local crystal field, leading to inhomogeneous broadening of the ensemble transitions. For a dopant concentration of 0.005%, this material has an exceptionally low inhomogeneous linewidth of 390 MHz, and can reach a narrow homogeneous linewidth of 73 Hz [38]

Each Er^{3+} ion substitutes for a Y^{3+} ion in one of two sites with C_1 rotational symmetry. Each of these two distinct sites is then divided into four orientation subsites, corresponding to the C_2 rotation and inversion symmetry. While, in general, these subsites are magnetically inequivalent, by aligning the magnetic field in the D_1–D_2 plane of the crystal, the magnetic equivalence can be restored [37]. The ground state $^4I_{15/2}$ and the first excited state $^4I_{13/2}$ of Er^{3+} ions consist of eight and seven Kramers doublets, respectively. These doublets become fully resolvable in the presence of a magnetic field.

The laser wavelength at 1536.3 nm coincides with the $^4I_{15/2} \leftrightarrow {}^4I_{13/2}$ transition in Er^{3+} for the first substitutional site of YSO. A double-passed acousto-optic modulator (AOM) is used to generate the pumping and input sequence. A fiber-coupled electro-optic modulation (EOM) shifts the laser frequency, and only the first-order sideband is transmitted through the subsequent etalon. A rapidly switchable neutral density filter (NDF) is used to attenuate the input pulses into single-photon level. The quarter waveplate adjacent to the crystal balances the absorption of the two polarizations of light. Three half-wave plates outside the cryostat compensate the phase error induced by the crystal and the quarter-wave plate (see Fig. 1(a)).

3. EFFECTIVE SPECTRAL TAILORING WITH PRACTICAL CONDITION

Some limitations of Er^{3+} ions in the communication band include the 10-ms excited-state lifetime and the branching ratio of less than 10% [33], which significantly reduce the performance of spin initialization and state manipulation, compared with other rare-earth ions [39]. Erbium-based quantum memories typically operate near the optical transition with the highest optical density—namely, the $^4I_{15/2} \rightarrow {}^4I_{13/2}$ transition with $\Delta m_I = 0$—which also exhibits the strongest transition dipole moment. This results in a near-unity branching ratio, ensuring that most spontaneous emission returns the atom to its initial ground-state manifold. Here, Z_1 is the lowest energy level of the crystal field Hamiltonian for $^4I_{15/2}$ and Y_1 is the lowest energy level of the crystal field Hamiltonian for $^4I_{13/2}$ (see Fig. 1(b)). A magnetic field is necessary to remove degeneracy, and improve coherence time and hole burning performance [40]. However, another challenge is that thermal phonons couple to electronic spins greatly reducing the hyperfine lifetime. An effective solution is to lower the temperature and increase the splitting [27]. Here, we demonstrate efficient spectral tailoring using more practical experimental conditions, i.e., using neither dilution refrigerators nor superconducting magnets.

A schematic of the experiment is shown in Fig. 1(a). Two N52 cube permanent magnets with dimension of 3/4 × 3/4 × 3/2 inch, separated by 4.5 mm, generate a uniform magnetic field of 1.1 T. In the regime of 0.9 K and 1.1 T, the hyperfine relaxation is mainly dominated by the one-phonon direct process [27]. The density of a phonon with energy equal to the electronic spin splitting $\hbar\omega_g = g\mu_B B$ follows the Planck distribution,

$$u(B,T) = \frac{\mu_B^3 g^3 B^3}{\pi^2 \hbar^2 c^3} \frac{1}{e^{\frac{\mu_B g B}{k_B T}} - 1}, \tag{1}$$

where B and g are the magnetic field and the g-factor along a specific axis, respectively; μ_B is the Bohr magneton, k_B is the Boltzmann constant, T is the temperature. The phonon distribution model in Fig. 1(c) reveals that the phonon density is relatively low in our experiment.

The phonon-mediated relaxation is obtained by measuring the lifetime of spectral holes. The spectral hole burning achieved using multiple burning cycles each consists of a train of 1-MHz-bandwidth pumping pulses, a pump-off duration ($\Delta t_{\text{in-loop}}$) of 10 ms of each cycle. The delay after pumping cycle ($\Delta t_{\text{out-loop}}$) is also controlled to optimize the optical density and noise. The spectral hole lifetime with varying pumping cycles is shown in Figs. 2(a) and 2(b). During the hole-burning process, the excited ions will mostly decay back to the original ground hyperfine state [Fig. 1(b)] due to the small branching ratio. We have realized that continuous pumping, as traditionally employed, results in inefficient pumping. This is due to the reduced branching ratio induced by stimulated emission.

By optimizing the pumping cycle, i.e., introducing optimum delay times when the pump is switched off, we obtain an efficient hole burning process. For a single hole, this is achieved using two monochromatic square pulses with varying duration (0.05–1 ms) and time separation (0–10 ms). Figure 2(a) presents experimental evidence of this process. The hole area is recorded using two pump pulses of approximately 0.05-ms duration, separated by varying time intervals. As the separation between the pulses increases, the hole area grows, indicating improved pumping efficiency, and eventually saturates at a time scale of approximately 10 ms, consistent with the excited-state decay time. We then measure the pumping efficiency after applying between 1 and 300 pump pulses, followed by a delay period to allow the excited atoms to decay (out-loop delay). Figure 2(b) shows the resulting permanent spectral hole and quantifies its efficiency as a function of the number of pumping cycles. Here, we define hole depth as the difference in optical density (OD) before and

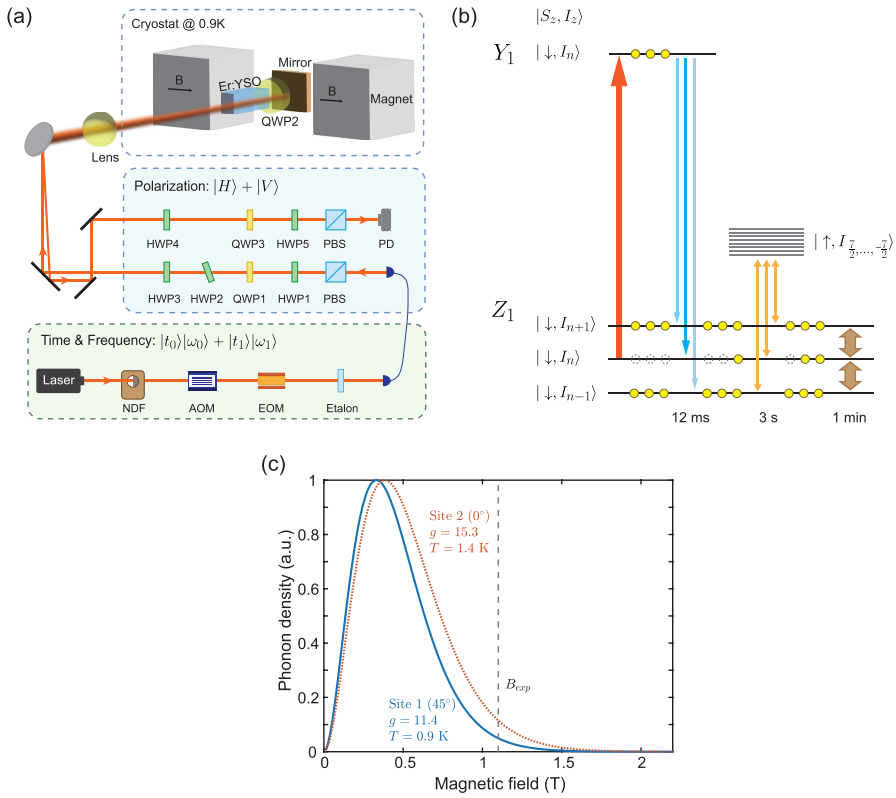

Fig. 1. (a) Schematic of the experimental system. A $^{167}Er^{3+}$:YSO crystal is situated in a uniform magnetic field of 1.1 T generated by two permanent magnets, and placed within a 0.9-K cryostat. A double-passed acousto-optic modulator (AOM), a fiber-coupled electro-optic modulation (EOM), and an Etalon generate the time and frequency entangled state. A series of half- and quarter-wave plates (HWP, QWP) encode and decode the polarization information. A rapidly switchable neutral density filter (NDF) attenuates the input pulses down to single-photon level. (b) Illustrations of hyperfine-level population relaxation mechanism. A spectral hole near the $Z_1{:}S_\downarrow I_n \rightarrow Y_1{:}S_\downarrow I_n$ $(n = -\frac{7}{2}, \ldots, \frac{7}{2})$ transition is burnt by a pump pulse (red). The hole is eliminated over time by spontaneous decay (blue) with a lifetime of approximately 12 ms, one-phonon direct relaxation (orange) of 3 s, and hyperfine cross-relaxation (brown), which is expected to be approximately 1 min. (c) The theoretical model describes the thermal phonon distribution at the current experimental condition (blue solid) and the experimental condition in Rančić *et al.* (orange dotted) [27]. The magnetic field on the horizontal axis corresponds to the phonon energy matching the ground electronic spin splitting.

after hole burning. The hole depth indicates the efficiency of the optical pumping. After the hole burning process is done, the hole decay is dominated by phonon relaxation between the hyperfine levels. Two exponential fits to the spectral hole decay reveal that the lifetimes of spontaneous decay (τ_1) and phonon-mediated decay (τ_2) are 12 ms and 3 s, respectively, and 92% ions are well initialized into other hyperfine states [27]. The coherence time of the optical transition is measured to be $T_2 = 169\,\mu$s by the Hahn echo method. The effective spectral tailoring permits a variety of memory protocols applied in C-band solid-systems in a more practical experimental condition.

By further increasing the magnetic field, for example, using Halbach array or wedge-composed magnets, the phonon-mediated relaxation can be fully suppressed and atomic polarization can be achieved with nearly 100% efficiency, which can result in a hole lifetime of 1 min limited by the hyperfine cross-relaxation [27].

To model the effect of interleaved pumping, we consider a three-level atomic system with ground states $|1\rangle$ and $|2\rangle$, and excited state $|3\rangle$. The system is driven by a laser field on the $|2\rangle \leftrightarrow |3\rangle$ transition, and decays spontaneously from $|3\rangle \rightarrow |2\rangle$ at rate γ_{32} and from $|3\rangle \rightarrow |1\rangle$ at rate γ_{31}. The population decay rate of $|2\rangle \leftrightarrow |1\rangle$ states is γ_{21}. The time evolution of the populations $\rho_{ii}(t)$ is governed by the following differential equations:

$$\frac{d\rho_{11}}{dt} = \gamma_{21}(\rho_{22} - \rho_{11}) + \gamma_{31}\rho_{33}, \tag{2}$$

$$\frac{d\rho_{22}}{dt} = \gamma_{21}(\rho_{11} - \rho_{22}) + \gamma_{32}\rho_{33} + R_{23}(t)(\rho_{33} - \rho_{22}), \tag{3}$$

$$\frac{d\rho_{33}}{dt} = -(\gamma_{32} + \gamma_{31})\rho_{33} - R_{23}(t)(\rho_{33} - \rho_{22}), \tag{4}$$

where the effective coupling rate $R_{23}(t)$ due to coherent driving is given by $R_{23}(t) = 2\Omega_{23}(t)^2/(\gamma_{21} + \gamma_{32})$.

In the interleaved pumping scheme, the pump is switched off periodically for approximately 10 ms (in-loop delay) allowing atoms to decay with a higher probability to the shelved state. The theoretical and experimental results in Fig. 2 show that, for a fixed total pumping duration, interleaved pumping leads to higher pumping efficiency compared with continuous driving. The model prediction in Figs. 2 (c) and 2(d) obtained from Eqs. (2)–(4) indicates that a continuous 50-ms pump is less effective than a sequence of fifty 1-ms pulses, separated by 10 ms to allow for atoms to decay before repumping. Ideally, continuous pumping over an extended period—of the order of the ground-state

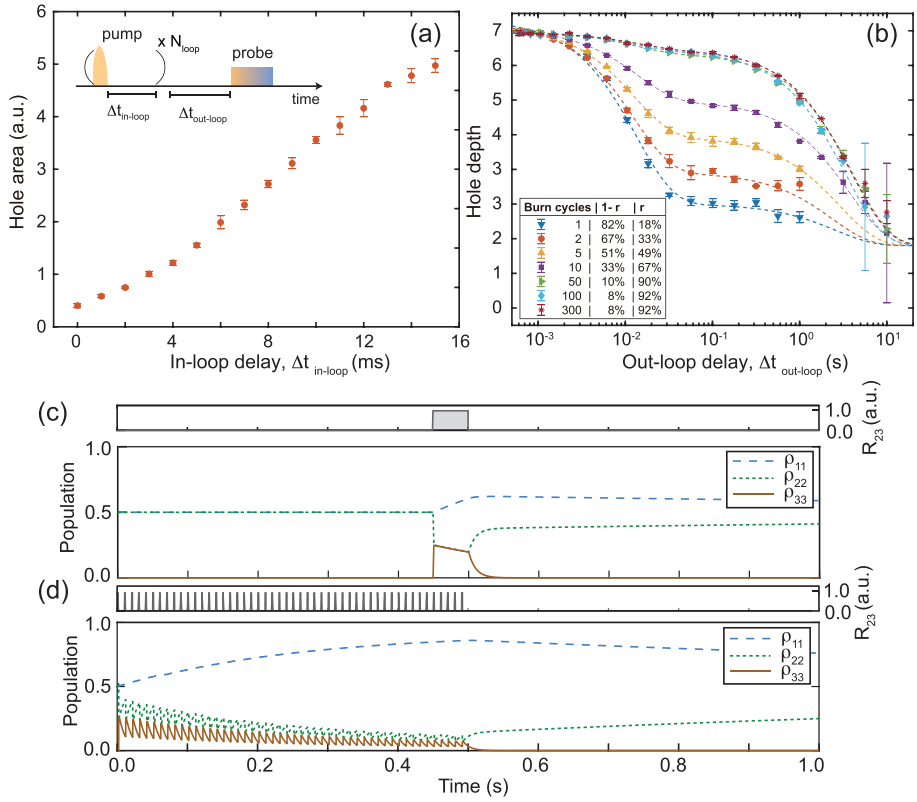

Fig. 2. (a) Integrated area under the spectral hole, which is proportional to light transmission, as a function of the in-loop delay between two pumping pulses, with an out-loop delay of 1 ms. Here, two pumping pulses of width 0.05 ms were used. Inset shows the hole burning sequence for the hole lifetime measurement in panels (a) and (b). Error bars are derived from four data sets. (b) Hole depth (see text for definition) reduces over time with varying hole-burning cycles. A double-exponential fit of the form $f(t) = a_1 e^{-t/\tau_1} + a_2 e^{-t/\tau_2} + C$ is used to extract lifetimes $\tau_1 = 12$ ms and $\tau_2 = 3$ s corresponding to spontaneous emission and phonon-mediated hyperfine decay. The ratio $r = a_2/(a_1 + a_2)$ describes the atomic polarization fidelity. Theoretical plot of atomic populations as a function of time for (c) continuous pumping of 50 ms and (d) interleaved pumping using fifty 1-ms pulses are shown. The rate R_{23} is plotted above each graph. In this simulation, we consider a ground state decay time ($T_1 = 2\pi/\gamma_{21}$) of 3 s, excited state decay time of $2\pi/(\gamma_{31} + \gamma_{32}) = 10$ ms, and branching ratio of $\gamma_{32}/\gamma_{31} = 0.9$.

lifetime (3 s)—can achieve high-efficiency population transfer. However, such long-duration pumping introduces significant pump-induced heating, leading to a noticeable increase in the crystal temperature. When the total pumping time is limited, the coupling rate R_{23} can effectively drive stimulated emission from the excited state back to the initial ground state, thereby reducing the overall pumping efficiency.

4. EFFICIENT AFC PREPARATION

To efficiently create atomic frequency combs, a sequence of pumping pulses with varying frequencies is employed as in Fig. 3(a). Single or multiple AFC windows were created by sweeping the pump frequency over the corresponding frequency window. The pumping cycle consists of a set of complex hyperbolic secant pulses that exhibit a square frequency spectrum, followed by an in-loop delay [41,42].

Multiple pumping parameters including the power, bandwidth and duration of pump pulse, in-loop delay, and pump loops were scanned to optimize storage efficiency. Figure 3(b) shows the integrated hole area, indicating the efficiency of the hole burning, for different in-loop delays, as an example. At the end of the pumping cycle, an out-loop delay is applied to allow excited atoms to decay prior to the input qubits. As shown in Fig. 3(c), the spontaneous emission noise is negligible after 50 ms. The storage efficiency up to 6.1% and 5.0% for a classical and single-photon pulse, respectively, is observed with an out-loop delay of 100 ms. This represents an enhancement of more than an order of magnitude compared with previous work, where a low magnetic field was used [43,44].

For atomic frequency combs with square comb profiles created by adiabatic pulses, the storage efficiency can be estimated using the following equation [42,45]:

$$\eta = \frac{d^2}{F^2}\exp(-\frac{d}{F})\mathrm{sinc}^2(\frac{\pi}{F})\exp(-d_0), \tag{5}$$

where d is the optical depth (OD) of the atomic medium before optical pumping, F is the finesse of the combs, and d_0 is the OD corresponding to the background absorption after spectral tailoring.

Considering a fixed optical depth d, different pumping protocols can affect the background absorption and the AFC finesse. In our case, the OD is approximately $d \sim 3.3$ at an out-loop delay of approximately 50 ms. The interleaved pumping returns a comb finesse of approximately $F \sim 3$ and a background absorption OD of $d_0 \sim 1.3$. The theoretically estimated efficiency is approximately 7.5%, which aligns with the measured efficiency

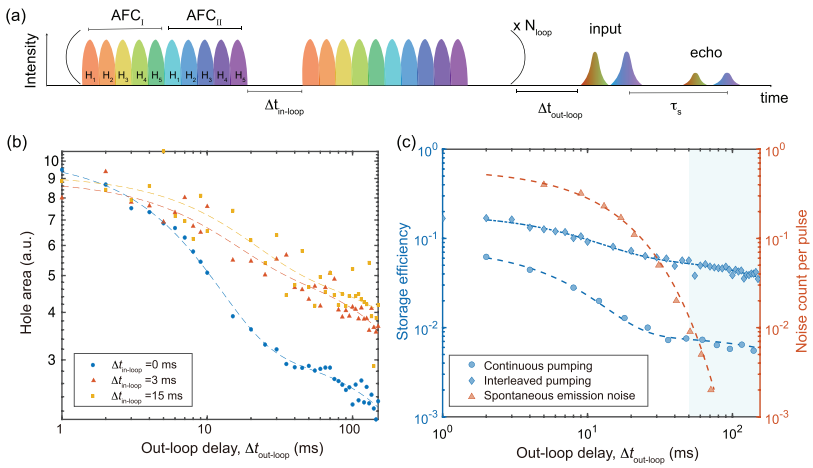

Fig. 3. (a) Schematic of the interleaved optical pumping sequence for spectral tailoring of the atomic spectrum. The system includes five parameters to be optimized; the pump power, duration, and spectral width of each hole H_i, the number of batches performed N_{loop}, and the delay time between each batch of pulses $\Delta t_{in-loop}$. After preparation, the system simultaneously stores two qubits encoded on multiple degrees of freedom for a time τ_s. (b) By varying the in-loop delay, an efficient optical pumping cycle, measured by the area under the hole, is obtained. Choosing an optimal set of pumping parameters maximizes the spectral tailoring, which improves storage efficiency. (c) Blue, the AFC memory efficiency with interleaved (diamond) or continuous (circle) pumping versus waiting time, $\Delta t_{out-loop}$, after pump. Orange, average noise photon counting due to the spontaneous emission from the excited state. For $\Delta t_{\text{out-loop}}$>50 ms, the spontaneous emission noise is found to be negligible (shaded region). Here, the AFC bandwidth used is 16 MHz. Dashed lines in (b) and (c) are double-exponential fits.

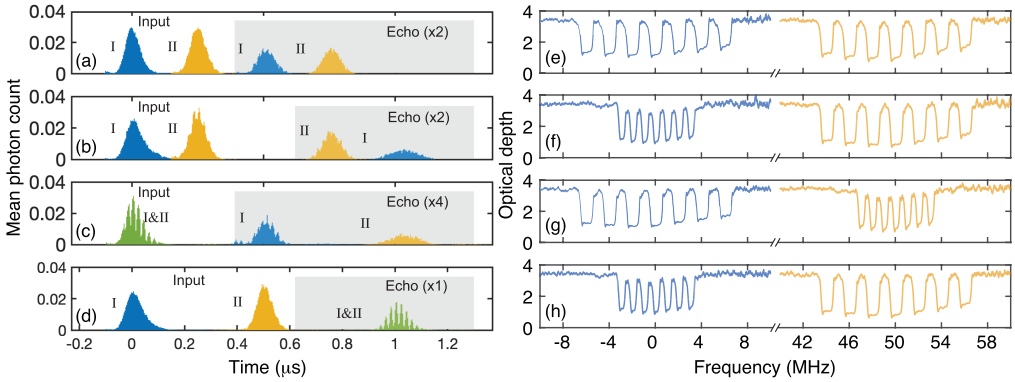

Fig. 4. Memory performance at the single-photon level. Coherent control over the storage of photons with two degrees of freedom, frequency, and time is shown. By burning spectrally separated AFC structures with varying parameters (right column), independent modulation of the storage time of each photon is achieved (left column). By storing qubits of varying frequency for different durations, we perform pulse processing, including (a,e) FIFO storage, (b,f) FILO storage, and (c,d,g,h) frequency-dependent delay. I and II refer to the first and second time-bin of input and echo light pulses.

of 6%, considering the uncertainty in the OD estimation. Experimentally, we observed [see Fig. 4(c)] that interleaved pumping results in an approximately 8-fold enhancement in efficiency compared with the traditional continuous pumping method.

5. MULTIDIMENSIONAL QUANTUM STORAGE

To demonstrate the compatibility of multiple degrees of freedom (DOFs) of photonic qubits with the memory, we performed multidimensional storage experiments encoded with frequency, time, and polarization qubits. The time and frequency qubit is encoded by the AOM and EOM in Fig. 1(a). A 1-GHz-wide etalon selects the desired sideband of the EOM. Optical pulses with two orthogonal polarization states interact symmetrically with the ions in the crystal, facilitated by QWP2 and the mirror behind the crystal, which retroreflects the light back into the medium. The HWP3 and HWP4 align the light's polarization to the crystal axis which is birefringent. A tilted 0° HWP2 compensates the phase difference of the two polarizations. Then, the two PBS–HWP–QWP combinations enable generation and projection measurement of polarization on the $\{|H\rangle, |V\rangle, |D\rangle = \frac{1}{\sqrt{2}}(|H\rangle + |V\rangle), |R\rangle = \frac{1}{\sqrt{2}}(|H\rangle - i|V\rangle)\}$ basis.

The frequency and time-bin storage is shown in Fig. 4. Two AFC windows of bandwidth 8 MHz and 16 MHz separated by 50 MHz are prepared near the central peak of the absorption spectrum. The storage times are 0.5 μs and 1 μs, which are modest for an input pulse of 100 ns. The input pulses at the two time-bins have different center frequencies matching those of two AFCs, each containing five spectral holes (combs). The delay can be designed for each AFC to retrieve the two time-bin data in either first-in–first-out (FIFO) or first-in–last-out (FILO) order. The frequency bins can be coherently separated (interfered) when

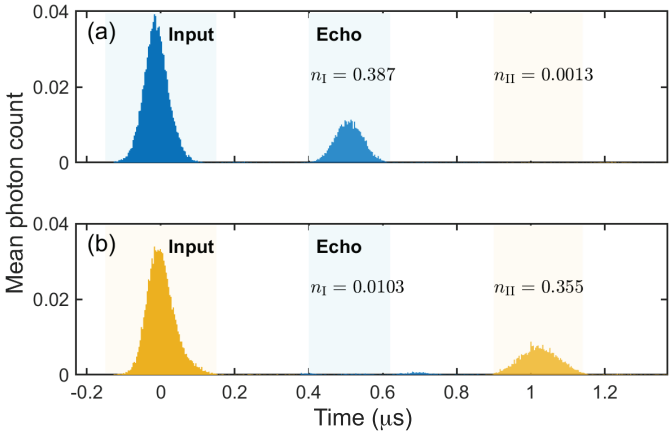

Fig. 5. Time-resolved frequency-dependent memory. Two weak coherence pulses with single but different frequency are injected to an AFC memory as shown in Fig. 4(g). The mean photon count shown on the figure for different time bins corresponding to different frequency bins exhibit a time-bin and frequency storage fidelity of 99.7% and 97.5%.

they enter the memory at the same (different) time-bins. This frequency-dependent delay can be used to coherently process qubits with a frequency difference indistinguishable by gratings or other conventional frequency processors. The slightly broadened echos with 1 μs storage time in Figs. 4(b) and 4(c) are due to the narrower corresponding AFC bandwidth. The imperfect input interference fringes in Fig. 4(c) are caused by the etalon leakage (0.9%) of the 4-GHz EOM sideband.

The intensity noise of time and frequency qubits is evaluated by designing a time-resolved frequency-dependent memory, where an AFC as shown in Fig. 4(g) is created and a single-frequency input pulse is injected to the memory. The result is shown in Fig. 5. Since the single-photon detector cannot distinguish a multi-photon event, the mean photon count n is deduced from the measured count n' using the Poisson distribution: $n' = \sum_{k>0} \frac{e^{-n} \cdot n^k}{k!}$, where the summation is over photon numbers k>0. Fidelities of 99.7% and 97.5% obtained from the intensity measurements demonstrate excellent time-bin and frequency performance, indicating low noise, negligible second AFC echo, and absence of frequency cross talk.

To evaluate the performance of the memory for storage of an arbitrary polarization state, we performed quantum process tomography of the quantum memory. The goal of process tomography is to find the map that corresponds to an arbitrary, unknown process. Generally, this corresponds to determining some coefficient of matrix χ for a specified set of basis operators $\{A_n\}$, representing a map as

$$\mathcal{E}(\rho) = \sum_{n,m} \chi_{nm} A_n \rho A_m^{\dagger}. \tag{6}$$

To determine χ from the experimental data, we employ a standard minimum-value optimization procedure [46] for both a photodiode and a single-photon measurement. In the case of the photodiode measurement, input pulses are similar in amplitude to the pump field to produce the AFC. For the single-photon operation, the input pulses are attenuated to fewer than one photon per shot. We perform sixteen measurements for four orthogonal polarization states: $\{|H\rangle, |V\rangle, |D\rangle, |R\rangle\}$. Three half-wave plates are used to compensate the phase difference between 2 polarizations caused by the crystal. To evaluate the accuracy of the memory process, we compute the process fidelity of the resulting map as $\mathcal{F} = \mathrm{Tr}(\sqrt{\sqrt{\chi_{exp}}\chi_{ideal}\sqrt{\chi_{exp}}})^2$. For a memory process, the input state should remain unchanged, so the ideal χ matrix has a unit value for the identity term and zero elsewhere, corresponding to the map $\mathcal{E}_{ideal}(\rho) = I\rho I^{\dagger}$, where we choose an operator basis of Pauli operators $\{I, \sigma_x, -i\sigma_y, \sigma_z\}$ [47], or a matrix with $\chi_{00} = 1$ and zeros elsewhere.

Tomography was completed for the simultaneous storage of two pulses at different time bins, separated in frequency by 50 MHz and stored for 0.5 μs, as shown in Fig. 4(a). The tomography of the classical echos showed a process fidelity of 94.9% for the first pulse and 97.6% for the second pulse. Figure 6 shows the χ matrix elements for the single-photon tomography; in this case, the first echo demonstrated a process fidelity of 92.3%, while the second echo had a slightly improved fidelity of 95.5%. The difference in fidelity of storage in these two cases is due to the decreased interaction strength between the atoms and optical pulses of varying frequencies. The largest non-identity component for the two pulses was the ZZ-component for the first echo, with a magnitude of 0.032. However, both maps had small but non-negligible complex components associated with the off-diagonal elements IX, IZ (largest amplitude $0.123i$). These components were matched with the conjugated values for the XI and ZI components, which suggests that the angled quarter-wave plate was insufficient to remove all phase effects. In particular, the magnitude of these components varies between the first and second echo, with the first echo having a more pronounced rotation.

6. DISCUSSION

There exist a number of avenues by which the performance of the system can yet be improved. Adjusting the optical path through the cryostat can improve polarization-qubit storage fidelity by removing dielectric-induced birefringence from the mirrors. By better aligning the magnetic field with respect to the D_1 and D_2 axes or using site 2 ions of Er:YSO, a larger magnetic g-factor can be achieved [37], leading to an enhanced ground-state lifetime and spectral tailoring. Furthermore, the magnitude of the magnetic field may be improved by focusing the field through a set of wedges composed of a magnetic material. Such elements could be incorporated directly into the mounting system for the crystals inside the cryostat. In addition, host crystals with low densities of nuclear spins such as $CaWO_4$ can be used to further increase the ground-state lifetime and optical coherence time of erbium ions.

The spin polarization initialization method [34] can be incorporated with the interleaved pumping scheme developed here to further enhance the memory performance [48]. With the ground-state lifetime being extended to 10 s, more efficient spectral tailoring can be achieved to reduce background absorption OD below 0.2, which can further increase the storage efficiency, exceeding 30%. Due to the inhomogeneous broadening of the optical transitions of erbium ions in a YSO crystal, a memory bandwidth of 500 MHz can be created, which can be integrated with entangled photon pairs generated by spontaneous parametric downconversion or four-wave-mixing processes to form an efficient light–matter interface [29]. At higher magnetic fields (produced by superconducting magnets), coherence times over one second have been demonstrated [27]. A similar regime can be accessed by engineering stronger permanent

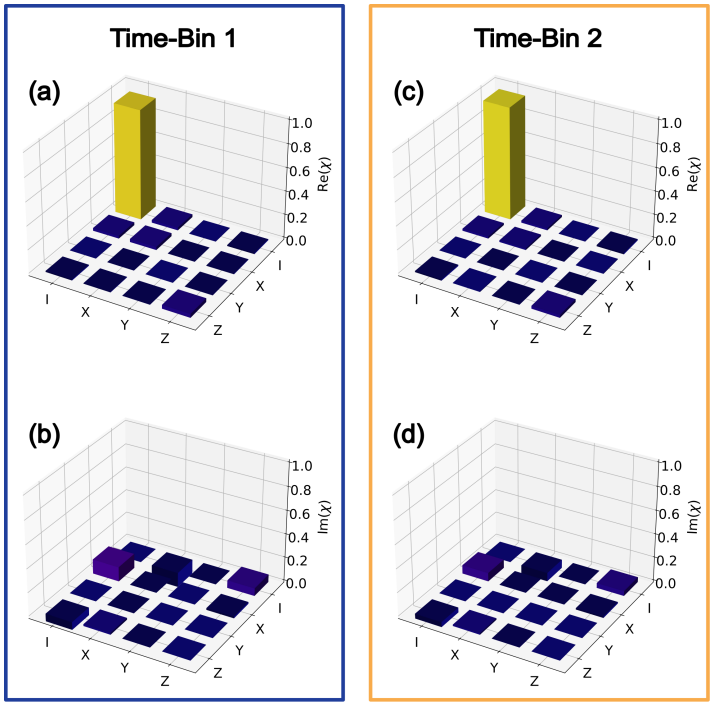

Fig. 6. Real and imaginary components of the reconstructed process matrix for time-bin 1 (blue) and time-bin 2 (yellow) after a 0.5-μs storage. The real components of the process matrices in panels (a) and (c) are near unity for both echos, demonstrating high polarization stability during storage. The imaginary components of the process matrix contains nonzero elements, indicating the system acquires an uncompensated phase during the storage process.

magnets. When combined with spin-wave storage [49], such conditions will enable the realization of long-lived quantum memories. Both directions are the focus of ongoing and future work. Moreover, the quantum memory devices with two frequency windows can be used for coherent processing of time- and frequency-bin qubits as well as storage of hyper-entangled photons with frequency, polarization, time, and number basis. In addition, multiple frequency windows can be created to store photons encoded with high-dimensional frequency-bins [50], by doping erbium ions into silica fibers or $LiNbO_3$, with much larger inhomogeneous broadening above 10 GHz [12,36].

7. CONCLUSION

In conclusion, we have developed the interleaved pumping scheme to effectively and efficiently prepare atomic frequency comb in a telecom compatible erbium-doped crystal. Importantly, we demonstrate efficiency enhancement by more than an order of magnitude compared with previous work in similar experimental conditions. We illustrate this effect with an Er:YSO crystal under a moderate temperature and magnetic field environment from a table-top cryostat and monolithic rare-earth magnets. Moreover, we demonstrate storage of multidimensional qubits in frequency, time, and polarization basis with high fidelity.

Funding. National Science Foundation (2410054); U.S. Department of Energy (3ERKJ381).

Acknowledgment. We wish to acknowledge Ali N Amiri for help with preparation of the millimeter-scale quarter-wave plate.

Disclosures. The authors declare no conflicts of interest.

Data availability. Data underlying the results presented in this paper are not publicly available but may be obtained from the corresponding author upon reasonable request.

REFERENCES

1. H. J. Kimble, "The quantum internet," Nature **453**, 1023–1030 (2008).
2. S. Wehner, D. Elkouss, and R. Hanson, "Quantum internet: A vision for the road ahead," Science **362**, eaam9288 (2018).
3. H.-J. Briegel, W. Dür, J. I. Cirac, *et al.*, "Quantum repeaters: the role of imperfect local operations in quantum communication," Phys. Rev. Lett. **81**, 5932–5935 (1998).
4. L.-M. Duan, M. D. Lukin, J. I. Cirac, *et al.*, "Long-distance quantum communication with atomic ensembles and linear optics," Nature **414**, 413–418 (2001).
5. Y. Lei, F. K. Asadi, T. Zhong, *et al.*, "Quantum optical memory for entanglement distribution," Optica **10**, 1511–1528 (2023).
6. S. Muralidharan, L. Li, J. Kim, *et al.*, "Optimal architectures for long distance quantum communication," Sci. Rep. **6**, 20463 (2016).
7. D. Awschalom, K. K. Berggren, H. Bernien, *et al.*, "Development of quantum interconnects (QuICs) for next-generation information technologies," Prx Quantum **2**, 017002 (2021).
8. K. Azuma, S. E. Economou, D. Elkouss, *et al.*, "Quantum repeaters: From quantum networks to the quantum internet," Rev. Mod. Phys. **95**, 045006 (2023).
9. Y. Ma, Y.-Z. Ma, Z.-Q. Zhou, *et al.*, "One-hour coherent optical storage in an atomic frequency comb memory," Nat. Commun. **12**, 1–6 (2021).
10. C. Simon, H. De Riedmatten, M. Afzelius, *et al.*, "Quantum repeaters with photon pair sources and multimode memories," Phys. Rev. Lett. **98**, 190503 (2007).
11. T.-S. Yang, Z.-Q. Zhou, Y.-L. Hua, *et al.*, "Multiplexed storage and real-time manipulation based on a multiple degree-of-freedom quantum memory," Nat. Commun. **9**, 3407 (2018).
12. X. Zhang, B. Zhang, S. Wei, *et al.*, "Telecom-band–integrated multimode photonic quantum memory," Sci. Adv. **9**, eadf4587 (2023).

13. F. Gu, S. G. Menon, D. Maier, *et al.*, "Hybrid quantum repeaters with ensemble-based quantum memories and single-spin photon transducers," arXiv (2024).
14. Z.-Q. Zhou, C. Liu, C.-F. Li, *et al.*, "Photonic integrated quantum memory in rare-earth doped solids," Laser Photonics Rev. **17**, 2300257 (2023).
15. D. Lago-Rivera, S. Grandi, J. V. Rakonjac, *et al.*, "Telecom-heralded entanglement between multimode solid-state quantum memories," Nature **594**, 37–40 (2021).
16. X. Liu, J. Hu, Z.-F. Li, *et al.*, "Heralded entanglement distribution between two absorptive quantum memories," Nature **594**, 41–45 (2021).
17. S. E. Thomas, L. Wagner, R. Joos, *et al.*, "Deterministic storage and retrieval of telecom light from a quantum dot single-photon source interfaced with an atomic quantum memory," Sci. Adv. **10**, eadi7346 (2024).
18. F. Kaneda and P. G. Kwiat, "High-efficiency single-photon generation via large-scale active time multiplexing," Sci. Adv. **5**, eaaw8586 (2019).
19. F. Kaneda, F. Xu, J. Chapman, *et al.*, "Quantum-memory-assisted multi-photon generation for efficient quantum information processing," Optica **4**, 1034–1037 (2017).
20. R. Chrapkiewicz, M. Dąbrowski, and W. Wasilewski, "High-capacity angularly multiplexed holographic memory operating at the single-photon level," Phys. Rev. Lett. **118**, 063603 (2017).
21. E. Knill, R. Laflamme, and G. J. Milburn, "A scheme for efficient quantum computation with linear optics," Nature **409**, 46–52 (2001).
22. S. Zaiser, T. Rendler, I. Jakobi, *et al.*, "Enhancing quantum sensing sensitivity by a quantum memory," Nat. Commun. **7**, 12279 (2016).
23. W. Ding, W. Zhang, and X. Wang, "Quantum-memory-assisted precision rotation sensing," Phys. Rev. A **102**, 032612 (2020).
24. J.-M. Mol, L. Esguerra, M. Meister, *et al.*, "Quantum memories for fundamental science in space," Quantum Sci. Technol. **8**, 024006 (2023).
25. M. Guo, S. Liu, W. Sun, *et al.*, "Rare-earth quantum memories: The experimental status quo," Front. Phys. **18**, 21303 (2023).
26. M. Afzelius, C. Simon, H. De Riedmatten, *et al.*, "Multimode quantum memory based on atomic frequency combs," Phys. Rev. A **79**, 052329 (2009).
27. M. Rančić, M. P. Hedges, R. L. Ahlefeldt, *et al.*, "Coherence time of over a second in a telecom-compatible quantum memory storage material," Nat. Phys. **14**, 50–54 (2018).
28. J. V. Rakonjac, Y.-H. Chen, S. P. Horvath, *et al.*, "Long spin coherence times in the ground state and in an optically excited state of $^{167}Er^{3+}$: Y_2 SIO_5 at zero magnetic field," Phys. Rev. B **101**, 184430 (2020).
29. M.-H. Jiang, W. Xue, Q. He, *et al.*, "Quantum storage of entangled photons at telecom wavelengths in a crystal," Nat. Commun. **14**, 6995 (2023).
30. M. Le Dantec, M. Rančić, S. Lin, *et al.*, "Twenty-three–millisecond electron spin coherence of erbium ions in a natural-abundance crystal," Sci. Adv. **7**, eabj9786 (2021).
31. M. T. Uysal, Ł. Dusanowski, H. Xu, *et al.*, "Spin-photon entanglement of a single Er^{3+} ion in the telecom band," arXiv (2024).
32. N. T. Arnold, C. P. Lualdi, and M. E. Goggin, "All-optical quantum memory," in *Quantum Computing, Communication, and Simulation IV*, Vol. 12911 (SPIE, 2024), pp. 390–394.
33. S. Hastings-Simon, B. Lauritzen, M. U. Staudt, *et al.*, "Zeeman-level lifetimes in Er^{3+}: Y_2 SiO_5," Phys. Rev. B **78**, 085410 (2008).
34. J. S. Stuart, M. Hedges, R. Ahlefeldt, *et al.*, "Initialization protocol for efficient quantum memories using resolved hyperfine structure," Phys. Rev. Res. **3**, L032054 (2021).
35. I. Craiciu, M. Lei, J. Rochman, *et al.*, "Nanophotonic quantum storage at telecommunication wavelength," Phys. Rev. Appl. **12**, 024062 (2019).
36. S.-H. Wei, B. Jing, X.-Y. Zhang, *et al.*, "Quantum storage of 1650 modes of single photons at telecom wavelength," npj Quantum Inf **10**, 19 (2024).
37. Y. Sun, T. Böttger, C. Thiel, *et al.*, "Magnetic g tensors for the $^4I_{15/2}$ and $^4I_{13/2}$ states of Er^{3+}: Y_2 SIO_5," Phys. Rev. B **77**, 085124 (2008).
38. T. Böttger, Y. Sun, C. Thiel, *et al.*, "Spectroscopy and dynamics of er $^{3+}$: Y_2 SIO_5 at 1.5 μ m," Phys. Rev. B **74**, 075107 (2006).
39. B. Lauritzen, S. Hastings-Simon, H. De Riedmatten, *et al.*, "State preparation by optical pumping in erbium-doped solids using stimulated emission and spin mixing," Phys. Rev. A **78**, 043402 (2008).
40. T. Böttger, C. Thiel, Y. Sun, *et al.*, "Optical decoherence and spectral diffusion at 1.5 μ m in Er $^{3+}$: Y_2 SIO_5 versus magnetic field, temperature, and Er^{3+} concentration," Phys. Rev. B **73**, 075101 (2006).
41. J. Minář, N. Sangouard, M. Afzelius, *et al.*, "Spin-wave storage using chirped control fields in atomic frequency comb-based quantum memory," Phys. Rev. A **82**, 042309 (2010).
42. P. Jobez, N. Timoney, C. Laplane, *et al.*, "Towards highly multimode optical quantum memory for quantum repeaters," Phys. Rev. A **93**, 032327 (2016).
43. S. Yasui, M. Hiraishi, A. Ishizawa, *et al.*, "Creation of a high-resolution atomic frequency comb and optimization of the pulse sequence for high-efficiency quantum memory in ^{167}Er: Y_2 SIO_5," Opt. Continuum **1**, 1896–1908 (2022).
44. I. Craiciu, M. Lei, J. Rochman, *et al.*, "Multifunctional on-chip storage at telecommunication wavelength for quantum networks," Optica **8**, 114–121 (2021).
45. M. Bonarota, J. Ruggiero, J.-L. Le Gouët, *et al.*, "Efficiency optimization for atomic frequency comb storage," Phys. Rev. A **81**, 033803 (2010).
46. J. L. O'Brien, G. J. Pryde, A. Gilchrist, *et al.*, "Quantum process tomography of a controlled-not gate," Phys. Rev. Lett. **93**, 080502 (2004).
47. I. L. Chuang and M. A. Nielsen, "Prescription for experimental determination of the dynamics of a quantum black box," J. Mod. Opt. **44**, 2455–2467 (1997).
48. E. Baldit, K. Bencheikh, P. Monnier, *et al.*, "Identification of λ-like systems in Er^{3+}: Y_2 SIO_5 and observation of electromagnetically induced transparency," Phys. Rev. B **81**, 144303 (2010).
49. B. Lauritzen, J. Minář, H. de Riedmatten, *et al.*, "Approaches for a quantum memory at telecommunication wavelengths," Phys. Rev. A **83**, 012318 (2011).
50. H.-H. Lu, M. Liscidini, A. L. Gaeta, *et al.*, "Frequency-bin photonic quantum information," Optica **10**, 1655–1671 (2023).